Journal of Materials Chemistry C

ROYAL SOCIETY OF CHEMISTRY

PAPER

View Article Online
View Journal | View Issue

Cite this: J. Mater. Chem. C, 2021, 9, 4206

Elimination of interlayer Schottky barrier in borophene/C_4N_4 vdW heterojunctions *via* Li-ion adsorption for tunneling photodiodes†

Cancan Zheng,[a] Cong Zhou,[a] Man Shi,[a] Haiyan Li,[a] Nianxi Dou,[a] Zhihao Ma,[a] Feifei Xia,[b] Yuanyuan He *[a] and Jianwei Zhao*[a]

Received 19th December 2020,
Accepted 30th January 2021

DOI: 10.1039/d0tc05943a

rsc.li/materials-c

The nonzero interlayer Schottky barrier leads to a compromise between photodetectivity and photoresponsivity in photodiodes based on vdW heterojunctions. Seeking for the appropriate vdW heterojunction with Ohmic contact and a high tunneling barrier is of great significance to realize high-performance photodiodes. We built borophene/C_4N_4 (B/C_4N_4) vdW heterojunctions with a reduced interlayer Schottky barrier, by combining density functional theory and non-equilibrium Green's function. The adsorption of Li-ions can further tune its Schottky contact into n-type Ohmic contact. The electronic properties of the Li-ion-adsorbed B/C_4N_4 vdW heterojunction, including the separation of hole–electron pairs, the work function, as well as the effective mass of carrier, can be modulated by changing the adsorption site of Li-ions. B/C_4N_4/Li shows the most excellent absorbing capability of the infrared illumination and the strongest negative rectification, due to the highest interlayer tunneling barrier. The bottom surface of the C_4N_4 sublayer is the optimal adsorption site of Li-ions, for the potential application of B/C_4N_4 vdW heterojunctions in tunneling photodiodes. Our work unveils the great significance of Li-ion adsorption in modulating the interlayer Schottky and tunneling barriers in vdW heterojunctions, thus improving their device performance.

1. Introduction

Semiconductor-based photodiodes, as a photoelectric sensing component to convert optical signals into photocurrent, has been widely studied and applied in many areas, such as image sensing, environmental monitoring, surveillance and spectroscopy.[1–4] Schottky barrier photodiodes are considered superior to p-i-n photodiodes, metal-semiconductor–metal photodiodes, and so on, in terms of their low power consumption, large current, and ultrahigh response speed.[5–8] Recently, van der Waals (vdW) heterostructures, which are formed by stacking different two-dimensional (2D) semiconductors vertically through vdW forces, have attracted the interest of a growing number of researchers. vdW heterojunctions have a large specific surface area, and their bandgap can be adjusted, while suppressing the recombination rate of the photogenerated carriers, which is greatly beneficial to the photoelectric process.[9] Unfortunately, the interlayer Fermi level pinning effect in vdW heterojunctions often leads to Schottky barriers at the interface and thus probably results in undesirable large contact resistance.[10] As a result, an inevitable compromise between photodetectivity and photoresponsivity often emerges in Schottky barrier photodiodes based on vdW heterojunctions.[11] In 2017, Zhai's group demonstrated the main positive contribution of high tunneling barrier to the high photocurrent, on the basis of which a highly sensitive WSe_2/SnS_2 photodiode was fabricated, exhibiting both ultrahigh photodetectivity of 1.29×10^{13} Jones (I_{ph}/I_{dark} ratio of $\approx 10^6$) and photoresponsivity of 244 A W^{-1} at a reverse bias under the illumination of 550 nm light (3.77 mW cm^{-2}).[12] Hence, seeking for the appropriate vdW heterojunction with Ohmic contact and a high tunneling barrier is of great significance to construct high-performance photodiodes.

Monolayer C_4N_4, as a novel p-type semiconductor, is competitive in the construction of vdW heterojunctions for applications in nanoscale electronics and optoelectronics, since it is reported that the Ohmic contact between C_4N_4 and graphyne could improve the conductivity of Li–S battery electrodes.[13] Moreover, monolayer C_4N_4 is predicted to display a strong infrared

[a] College of Material and Textile Engineering, Key Laboratory of Yarn Materials Forming and Composite Processing Technology, Jiaxing University, Jiaxing, 314001, Zhejiang, People's Republic of China. E-mail: heyy@zjxu.edu.cn, jwzhao@zjxu.edu.cn
[b] School of Chemical and Environmental Engineering, Jiangsu University of Technology, Changzhou, 213001, Jiangsu, People's Republic of China

† Electronic supplementary information (ESI) available: Optimized geometries and electronic properties of Li-ion-adsorbed borophene and C_4N_4 monolayers. See DOI: 10.1039/d0tc05943a

response, opening the possibilities of C_4N_4-based vdW heterojunctions for tunneling photodiodes.[14] Yang *et al.* reported the fabrication of C_3N by polymerization of 2,3-diaminophenazine (DAP), in which both N and C atoms are distributed homogeneously.[15] They provided a feasible way to control the distribution of N atoms for improving the experimental methods of C_4N_4 synthesis. By comparing the cohesive energy per atom and the n-layer exfoliation energy per unit area, the C_4N_4 monolayer is more stable than many other carbonitride monolayers and can be easily prepared from its bulk forms using a similar experimental mechanical exfoliation method to that of graphene.[16–18] It is possible to prepare C_4N_4 monolayers by experiments successfully, even though they have not been achieved hitherto. To eliminate the Schottky barrier, theoretical assessments suggest that monolayer borophene can be used as a substitute for the traditional noble metal for contact with monolayer C_4N_4.[19] For building tunneling photodiodes based on vdW heterojunctions, doping control is critical to further reduce the interlayer Schottky barrier. Considerable time and effort have been expended to develop effective doping strategies, such as thickness engineering,[20,21] surface modifications,[22–24] atomic substitutions,[25–27] and mechanical strain,[28,29] however these are not applicable to vdW heterojunctions, due to their peculiar structures. Experimentally, ionic intercalations have been developed to complementarily dope vdW materials for diode devices, providing a potential method to realize tunneling photodiodes based on borophene/C_4N_4 (B/C_4N_4) vdW heterojunctions.[30]

In this study, based on density functional theory (DFT), we built B/C_4N_4 vdW heterojunctions by stacking monolayer borophene and C_4N_4 vertically and further decorating them with Li-ions. The electronic properties of free-standing borophene and C_4N_4 monolayers, including the separation of hole–electron pairs ($\Delta\rho$), work function ($\Delta\Phi$), and effective mass of carriers (Δm^*), are rationally modulated by the combination of vertical stacking and Li-ion adsorption. Most significantly, the interlayer Schottky contact in B/C_4N_4 vdW heterojunctions has been transformed into an Ohmic contact *via* the adsorption of Li-ions. By modulating Li-ions from the top to bottom site on B/C_4N_4 vdW heterojunctions, the increasing tunneling barrier will not only enhance the optical absorption in the entire infrared region, but also improve the negative rectification behavior. This work shows the great significance of Li-ion adsorption on modulating the interlayer energy barrier in vdW heterojunctions, paving the way towards applications in high-performance tunneling photodiodes.

2. Computational details

A vertical interface consisting of borophene and C_4N_4 monolayers, *i.e.* a B/C_4N_4 van der Waals (vdW) heterojunction, was built by matching the two crystals. For comparison, bilayer borophene and bilayer C_4N_4 were modeled as vdW homojunctions.[31–33] In the Atomistix-toolkit Virtual-nano-lab (ATK-VNL) package, the linear combination of atomic orbitals (LCAO) techniques was utilized to optimize the geometry of the stacking superlattice and to calculate its electronic properties.[34,35] A vacuum layer of about 25 Å was introduced to minimize the spurious interaction between neighboring layers. A specialized Grimme's approach (DFT-D3) was adopted to correct interfacial dispersion, taking van der Waals interactions into account.[36] The scalar-relativistic (SG15) optimized norm-conserving Vanderbilt (ONCV) pseudopotentials were employed with an energy cutoff of 100 Hartree, combined with the plane-wave basis set.[37] The *k*-point mesh of $10 \times 1 \times 10$ was selected in the Brillouin zone during geometric optimization. The position of the upper layer relative to the bottom layer was optimized until the energy and stress error were less than 1.0×10^{-3} eV Å^{-1} and 5.0×10^{-3} GPa, respectively. A much denser *k*-point mesh ($15 \times 1 \times 15$) was applied in the band structure and density of states (DOS) calculation. The electron–electron interactions were treated using the DFT-1/2 method considering the electron spin within Perdew–Burke–Ernzerhoff (PBE) parameterization, which has been widely applied to calculate the bandgap with more accuracy in a feasible time.[38,39]

Furthermore, the ballistic transport behavior of the two-probe B/C_4N_4 vdW heterojunction was systematically analyzed, by using DFT combined with the non-equilibrium Green's function (NEGF) method. Monolayer borophene with a length of 20.74 Å was used as the left electrode, whereas monolayer C_4N_4 with the same length was used as the right electrode. In the central region, monolayer borophene and C_4N_4 were stacked with each other with a length of 20.74 Å, which was further relaxed until the force on each atom was less than 0.5 eV. The wave functions and other physical operators are expanded with a double zeta polarized (DZP) LCAO basis and the fineness of the real space grid is determined by an equivalent plane wave cut-off of 100 Hartree. The current and transmission spectra were calculated by using the NEGF-implemented ATK-VNL package. The current was obtained by integrating the transmission within the bias window:[40,41]

$$I = \frac{e}{h}\int_{-\infty}^{+\infty} T(E)\left[f\left(\frac{E - E_F^L + eV_R}{k_b T_R}\right) - f\left(\frac{E - E_F^L + eV_L}{k_b T_L}\right)\right] dE, \quad (1)$$

where f is the Fermi function, E_F^L is the Fermi energy, T_L and T_R are the electron temperatures of the left and right electrodes and set as 300 K in this work, and V_L and V_R are the bias voltages applied to the left and right electrodes, respectively. $T(E)$ is the transmission coefficient around the Fermi level, describing the probability of an electron with a given energy (E) that transfers from the left electrode through the central region and into the right electrode.

3. Results and discussion

Among all possible allotropes in borophene, the free-standing β_{12} phase derived from the α-sheet structure is thermodynamically, mechanically, and dynamically the most stable.[42–44] In the following discussion, β_{12} borophene is chosen as the material to build a van der Waals heterojunction with C_4N_4 monolayers. As shown in Fig. 1a–e, monolayer borophene has a planar structure with anisotropic corrugation. The optimized constant lattices in

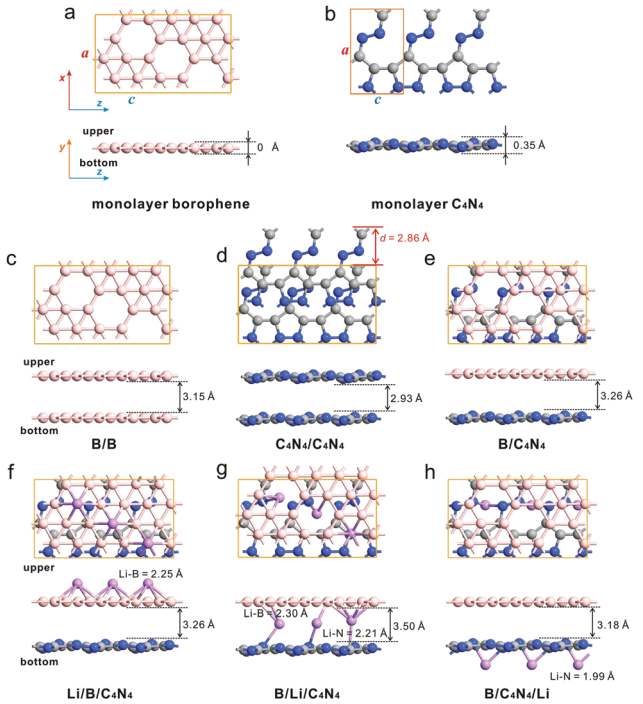

Fig. 1 Top and side views of free-standing (a) borophene and (b) C_4N_4 monolayers. Optimized configurations of (c) bilayer borophene (B/B), (d) bilayer C_4N_4 (C_4N_4/C_4N_4) as vdW homojunctions, and (e) B/C_4N_4 vdW heterojunctions. The lowest energy structures for Li-ion-decorated B/C_4N_4 vdW heterojunctions with (f) top, (g) sandwiched, and (h) bottom adsorption sites, respectively.

monolayer C_4N_4 are a = 6.08 Å and c = 3.58 Å, with a buckling height of ≈ 0.35 Å. During the formation of the B/C_4N_4 vdW heterojunction, we adapt the $\sqrt{2} \times \sqrt{10}$ borophene supercell to vertically stack with 1 × 3 C_4N_4, in which the corresponding mismatch of the lattice constants is less than 2%. There is an angle of 29.0° between the arrangement of vacancies and the z-direction in the monolayer borophene supercell. In the formed B/C_4N_4 vdW heterojunction, the relative position of borophene is freely relaxed, while the C_4N_4 sublayer remains frozen. After geometric optimization, the vertical distance between borophene and C_4N_4 is d_y = 3.26 Å. Compared with bilayer borophene (B/B) and bilayer C_4N_4 (C_4N_4/C_4N_4) as van der Waals (vdW) homojunctions (d_y = 3.15 and 2.93 Å, respectively), the above B/C_4N_4 vdW heterojunction possesses the widest interlayer distance. The binding energy (E_b) of the bilayer system is defined as:

$$E_b = (E_{upper+bottom} - E_{upper} - E_{bottom})/(N_B + N_C + N_N), \quad (2)$$

where $E_{upper+bottom}$, E_{upper}, and E_{bottom} are the relaxed energies of the bilayer system, and the isolated upper and bottom layers, respectively. N_B, N_C, and N_N are the number of boron atoms in the borophene supercell, and carbon and nitrogen atoms in the C_4N_4 supercell. The relevant results are listed in Table 1. It is indicated from the negative E_b (−0.10 eV per atom) that the B/C_4N_4 vdW heterojunction is energetically feasible and can be obtained easily, even though it is weaker than those in bilayer

Table 1 The lattice constants along the x (a) and z (c) directions, binding energy (E_b), and the interlayer distance (d_y) in B/B, C_4N_4/C_4N_4, and B/C_4N_4 bilayer systems before and after the adsorption of Li-ions, respectively. The nearest length of the Li–X bond in Li-adsorbed B/C_4N_4 vdW heterojunctions

Superlattice	a (Å)	c (Å)	E_b (eV per atom)	d_y (Å)	L_{Li-X} (Å)
B/B	5.86	10.13	−0.045[a]	3.15	—
C_4N_4/C_4N_4	6.08	10.77	−0.036[a]	2.93	—
B/C_4N_4	6.08	10.77	−0.010[a]	3.26	—
$Li/B/C_4N_4$	6.08	10.77	−0.22[b]	3.26	2.25 (Li–B)
$B/Li/C_4N_4$	6.08	10.77	−0.24[b]	3.50	2.30 (Li–B) 2.21 (Li–N)
$B/C_4N_4/Li$	6.08	10.77	−0.13[b]	3.18	1.99 (Li–N)

[a] Before Li-ions adsorption: $E_b = (E_{upper+bottom} - E_{upper} - E_{bottom})/(N_B + N_C + N_N)$, where $E_{upper+bottom}$, E_{upper}, and E_{bottom} are the relaxed energies of the bilayer systems, the isolated upper and bottom layers, respectively, and N_B, N_C, and N_N are the numbers of B atoms in the borophene supercell, and C and N atoms in the C_4N_4 supercell. [b] After Li-ion adsorption: $E_b = (E_{Li+B+C_4N_4} - N_{Li}E_{Li} - E_B - E_{C_4N_4})/(N_B + N_C + N_N + N_{Li})$, where $E_{Li+B+C_4N_4}$ denotes the total energy of Li-adsorbed B/C_4N_4 vdW heterojunctions, whereas E_{Li}, E_B, and $E_{C_4N_4}$ represent the total energies of isolated Li-ion, monolayer borophene and C_4N_4 supercells, respectively. N_{Li}, N_B, N_C, and N_N are the numbers of Li-ions, and B, C, and N atoms in a unit supercell of the adsorption system.

borophene and C_4N_4. The wider interlayer distance and smaller E_b value of the B/C_4N_4 vdW heterojunction than the corresponding homojunctions might be ascribed to the lower number of unpaired electrons.[45]

We further decorate Li-ions on the top, sandwiched, and bottom sites of the B/C_4N_4 vdW heterojunction, respectively. Li-ions are inclined to be adsorbed on the hollow site of the vacancies. By comparing Fig. 1f–h and Fig. S1 (ESI†), when Li-ions are adsorbed on the top and bottom sites of the B/C_4N_4 vdW heterojunctions (which are called $Li/B/C_4N_4$ and B/C4N4/Li for short, respectively), the lengths of the Li–B bond and Li–N bond are 2.25 and 1.99 Å, respectively, irrespective of the formation of B/C_4N_4 vdW heterojunctions. Meanwhile, the interlayer distance in B/C_4N_4 vdW heterojunctions is also insensitive to the adsorption of Li-ions. However, the insertion of Li-ions between borophene and C_4N_4 has expanded the interlayer distance by 7.36% from 3.26 Å to 3.50 Å. It is commonly believed that such an expanded bilayer, considered as an ideal structure for Li-ion batteries, can provide pathways for rapid electron transfer and further enhance the gravimetric and areal capacities.[46,47]

The stability of Li-ion adsorption on B/C_4N_4 vdW heterojunctions is evaluated by the binding energy (E_b) of each Li-ion according to the following formula:[48,49]

$$E_b = (E_{Li+B+C_4N_4} - N_{Li}E_{Li} - E_B - E_{C_4N_4})/(N_{Li} + N_B + N_C + N_N), \quad (3)$$

where $E_{Li+B+C_4N_4}$ denotes the total energy of B/C_4N_4 vdW heterojunctions with Li-ion adsorption, whereas E_{Li}, E_B, and $E_{C_4N_4}$ represent the total energies of isolated Li-ion, monolayer borophene and C_4N_4 supercells, respectively. N_{Li}, N_B, N_C, and N_N are the number of Li-ions, and B, C, and N atoms in a unit supercell of the adsorption system. Obviously, the adsorption of Li-ions on B/C_4N_4 is much stronger than the weak vdW interaction between borophene and

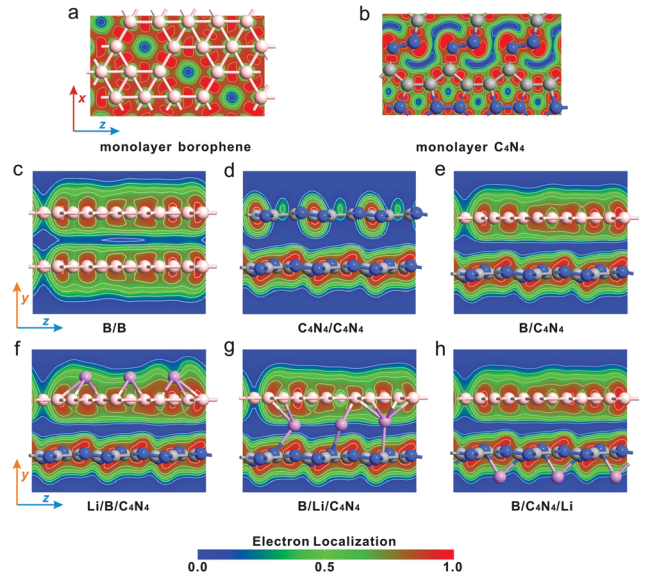

Fig. 2 Top views of ELF isosurfaces for (a) borophene and (b) C_4N_4 monolayers. Side views of ELF maps for (c) B/B, (d) C_4N_4/C_4N_4 vdW homojunctions, and (e–h) B/C_4N_4 vdW heterojunctions before and after Li-ion adsorption at the top, sandwiched, and bottom sites, respectively.

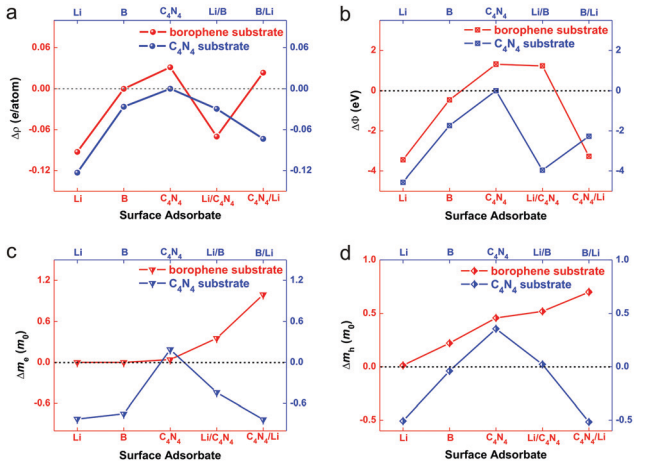

Fig. 3 (a) Mulliken charge transfer ($\Delta\rho$) between surface adsorbates and borophene (C_4N_4) substrates, (b) change of work function ($\Delta\Phi$), and (c and d) changes of electron effective mass (Δm_e) and hole effective mass (Δm_h) on borophene (C_4N_4) substrates at the GGA-1/2 level.

C_4N_4, as a strong ionic binding is brought about between the Li-ion and substrate. Bonding characteristics of B/C_4N_4 vdW heterojunctions can be revealed by analyzing the commonly used electron localization function (ELF), whose corresponding isosurfaces are shown in Fig. 2. In general, a large ELF value (>0.5) manifests a covalent bond, whereas the ionic bond is denoted by a smaller ELF value (<0.5).[50] Fig. 2a and b show the electron localization around B atoms in borophene and that around N atoms in a C_4N_4 monolayer. It could be found that in borophene, the B–B bonds far away from the vacancies are covalent, while those near the vacancies are ionic. There also exists a similar bonding characteristic in the C_4N_4 monolayer. Such coexistence of covalent and ionic bonds has resulted in their good structural stabilities. Fig. 2c–e demonstrate that the weak vdW forces play a key role in bilayer systems, as no strong bonds could be observed in the interface between borophene and C_4N_4. Furthermore, the adsorption of Li-ions on B/C_4N_4 vdW heterojunctions causes the formation of Li–B bonds on the top adsorption site and Li–N bonds on the bottom site with high ionization degree, similar to those in monolayer borophene and C_4N_4 in Fig. S2 (ESI†). Meanwhile, the interaction between borophene and C_4N_4 keeps control of the vdW forces. Different from the above two kinds of adsorption sites, the sandwiched Li–B and Li–N ionic bonds in $B/Li/C_4N_4$ vdW heterojunctions have effectively strengthened the interaction between borophene and C_4N_4.

The above bilayer systems before and after Li-ion adsorption can be classified into two types of adsorption systems, according to the type of substrate. Specifically, the borophene-substrate-systems consist of Li/B monolayer, B/B vdW homojunction, and B/C_4N_4, $B/Li/C_4N_4$, and $B/C_4N_4/Li$ vdW heterojunctions, in which Li-ions, borophene, C_4N_4, Li top-site-adsorbed C_4N_4 (Li/C_4N_4), and Li bottom-site-adsorbed C_4N_4 (C_4N_4/Li) monolayers are considered as the surface adsorbates. The cases of C_4N_4-substrate-systems are similar to the borophene-substrate-adsorption systems. Through this classification strategy, we explored the doping effect of various adsorbates on the electronic properties of borophene and C_4N_4 monolayers.

Mulliken charge densities in the above adsorption systems were calculated in Fig. 3a, to investigate the effect of vertical stacking and Li-ion adsorption on the interfacial separation of hole–electron pairs of bilayer structures. The electron density difference ($\Delta\rho$) is defined as follows:[51,52]

$$\Delta\rho(y)=\left(\int\rho_{\text{adsorbate+substrate}}(x,y,z)\mathrm{d}x\mathrm{d}z-\int\rho_{\text{adsorbate}}(x,y,z)\mathrm{d}x\mathrm{d}z-\int\rho_{\text{substrate}}(x,y,z)\mathrm{d}x\mathrm{d}z\right)\Big/N_{\text{substrate}}, \quad (4)$$

in which $\rho_{\text{adsorbate+substrate}}(x,y,z)$, $\rho_{\text{adsorbate}}(x,y,z)$, and $\rho_{\text{substrate}}(x,y,z)$ denote the electron densities of the adsorption system, the isolated adsorbate and substrate at the (x, y, z) point, respectively, and $N_{\text{substrate}}$ is the number of atoms in the substrate. All the adsorption systems are electrically neutral, as no external electric field is applied vertically. In Fig. 3a, a negative $\Delta\rho(y)$ indicates not only the electron accumulation on thte substrate but also the electron depletion on surface adsorbate, thus generating the separation of hole–electron pairs. In contrast, a positive $\Delta\rho(y)$ represents an opposite separation direction of hole–electron pairs. Conceptually, the amount of $\Delta\rho(y)$ can be employed to quantify the separation of hole–electron pairs.[53] In a unit supercell, each atom in C_4N_4 can draw 0.12 electrons from the adsorbed 3 Li atoms, leading to their ionization, which is much larger than that (0.093 e per atom) in Li-adsorbed borophene monolayers. The stronger electron-drawing capability of the C_4N_4 monolayer can also be reflected by the fact that each B atom in borophene has donated 0.032 electrons into C_4N_4 in the B/C_4N_4 vdW heterojunctions. This remarkable separation of

hole–electron pairs is probably attributed to both the electron-deficient property of B atoms in upper borophene and the electron-rich property of N atoms in bottom C_4N_4. In contrast, due to the nonexistence of interfacial charge transfer, it is difficult for hole–electron pairs to separate in B/B and C_4N_4/C_4N_4 vdW homojunctions, leading to their inapplicability in optoelectronics, which will be validated in the following optical absorption analysis. By changing the adsorption site of Li-ions on B/C_4N_4 vdW heterojunctions, it is observed that the amount of charge transfer between B/Li and C_4N_4 (−0.074 e per atom) is more than twice that between Li/B and C_4N_4 (−0.029 e per atom), indicating that the separation of hole–electron pairs between borophene and C_4N_4 can be enhanced by the sandwiched-site adsorption of Li-ions. Moreover, the adsorption of Li-ions on the bottom site can even reverse the separation direction of hole–electron pairs from −0.074 e per atom in B/Li/C_4N_4 to 0.024 e per atom in B/C_4N_4/Li. This is because the electron-drawing capability of C_4N_4 is so strong that it can accept not only the electrons from Li-ions but also those in borophene. Therefore, the carrier type and concentration on each sublayer of the B/C_4N_4 vdW heterojunctions can be modified by changing the adsorption site of Li-ions.

The variation of work function before and after surface adsorption will provide guidelines on how to tune the carrier concentration on borophene and C_4N_4 monolayers by the choice of surface adsorbate. The electrostatic potential calculations are performed to probe changes of the work function ($\Delta\Phi = \Phi_{adsorbate+substrate} - \Phi_{substrate}$) for borophene and C_4N_4 monolayers with different surface modifications.[54] The local density approximation (LDA) method predicted that the Φ values of isolated borophene, C_4N_4, and Li-ions are *ca.* 5.59, 7.12, and 2.29 eV, respectively. As shown in Fig. 3b, the formation of B/C_4N_4 vdW heterojunctions can decrease the work function of bottom C_4N_4 by 0.46 eV, meanwhile increasing that of upper borophene by 1.74 eV. As a result, n-type doping of C_4N_4 and p-type doping of borophene are effectively achieved. Conversely, the formation of B/B and C_4N_4/C_4N_4 vdW homojunctions has a negligible effect on the work function, owing to the minimum separation of hole–electron pairs. The adsorption of Li-ions may further change the work function in B/C_4N_4 vdW heterojunctions. For upper borophene, the adsorption of Li/C_4N_4 will increase its work function by 1.24 eV, whereas C_4N_4/Li can decrease its work function by 3.27 eV, showing an opposite doping effect. This is because the direct B–Li ionic bonds in B/Li/C_4N_4 are so strong that numerous electrons are donated from Li-ions to borophene, whereas electrons are accumulated on the C_4N_4 sublayer in B/C_4N_4/Li, because of the strong electron-donating capabilities of borophene and Li-ions. As for the C_4N_4 substrate, the adsorption of Li/B effectively decreases the work function by 3.96 eV, showing a stronger n-type doping effect than B/Li (−2.27 eV), due to the fact that borophene in B/Li/C_4N_4 shares a proportion of electrons injected from the inserted Li-ions.

The effective mass of carriers (m^*) is another critical factor to describe the influence of surface modification on the interfacial carrier transport in adsorption systems. m^* in the adsorption system is assessed by fitting parabolic functions to the conduction band bottom (valence band top) as follows:[55]

$$\frac{1}{m^*} = \frac{1}{h^2}\frac{\partial^2 E(k)}{\partial k^2}, \quad (5)$$

where k is the wave vector, and E_k is the energy corresponding to the wave vector k. The smaller effective masses of electrons (m_e)/holes (m_h) usually indicate the higher electron/hole mobility. Using the above method, m_e and m_h in the borophene monolayer are calculated to be $0.023m_0$ and $0.046m_0$, respectively, where m_0 stands for the mass of free-electrons. Such extremely high carrier mobility leads to the metallic property of pristine borophene. In the C_4N_4 monolayer, m_e is $0.84m_0$, much larger than $m_h = 0.52m_0$, exhibiting a p-type characteristic. Fig. 3c and d depict the change of effective mass of electron (Δm_e) and hole (Δm_h) in borophene and C_4N_4 substrate with various surface adsorbates. In B/C_4C_4/Li vdW heterojunctions, m_e and m_h on the borophene sublayer have reached $1.04m_0$ and $0.72m_0$, respectively, which are nearly 21.65 and 30.43 times larger than those in pristine borophene, showing the largest extent of reduction of the carrier mobility. It is speculated that in the meantime of carrier injection from C_4N_4/Li, a large number of scattering centers are also introduced into borophene, consequently impeding the carrier transport. The negligible interfacial separation of hole–electron pairs in B/B vdW homojunctions can reduce such carrier scattering, thus resulting in nearly zero Δm_e. However, the formation of C_4N_4/C_4N_4 vdW homojunctions has increased m_e and m_h by $0.19m_0$ and $0.36m_0$, respectively. It is attributed to the fact that the interlayer vacuum has blocked the carrier mobility between the upper and bottom C_4N_4 monolayers. In contrast, the remarkable separation of hole–electron pairs in B/C_4N_4 vdW heterojunctions has overwhelmed the blocking effect of interlayer vacuum. Hence, vertical stacking with borophene has a positive influence to improve the electron mobility of the C_4N_4 monolayer. In addition, the negative Δm_e and Δm_h in Li/B/C_4N_4 is nearly twice those in B/Li/C_4N_4, revealing that the adsorption of Li/B has promoted the carrier transport efficiency on the C_4N_4 substrate more dramatically.

Fig. 4a and b show the band structures of pristine borophene and C_4N_4 monolayer before and after Li-ion adsorption. The bands projected to borophene, C_4N_4 and Li-ions are indicated by red, blue, and yellow colors, respectively. Obviously, the electron-donating capability of Li-ions is so strong that their adsorption can effectively enhance the metallic property of borophene and even tune the C_4N_4 monolayer from p-type into metallic. The domination of interlayer vdW interaction in bilayer systems is quite different from the above ionic interaction in modulating the band structure. Fig. 4c demonstrates that the original band structures of pristine borophene and C_4N_4 monolayers are well preserved in B/B and C_4N_4/C_4N_4 vdW homojunctions, owing to the negligible separation of hole–electron pairs. In contrast, the strong separation of hole–electron pairs has enhanced the interlayer coupling effect and thus opened the bandgap of borophene to 0.18 eV. As a result, the band hybridization in the B/C_4N_4 vdW heterojunction is much stronger than those in the corresponding vdW homojunctions.

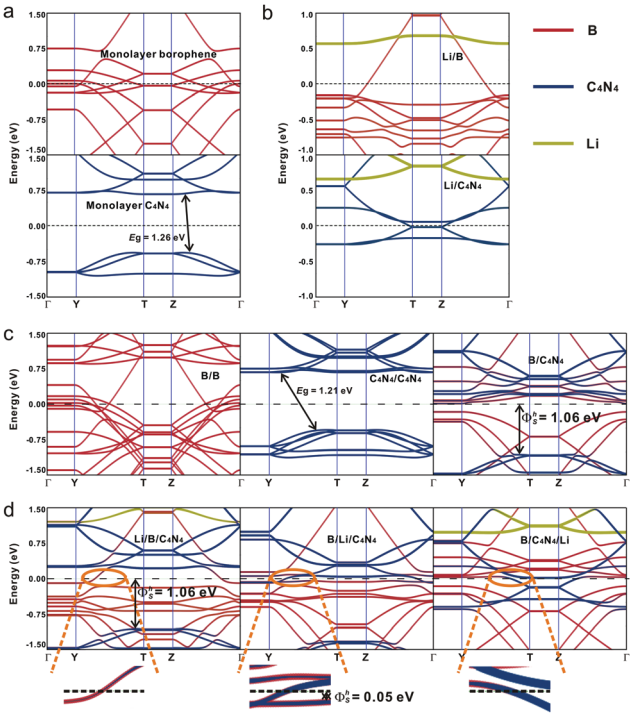

Fig. 4 Band structures for pristine borophene and C_4N_4 monolayers (a) before and (b) after Li-ion adsorption, (c) bilayer systems consisting of borophene and C_4N_4, and (d) B/C_4N_4 vdW heterojunctions with Li-ions at the top, sandwiched, and bottom sites, respectively. Red line: borophene; blue line: C_4N_4; yellow line: adsorbed Li-ions. The Fermi level is set at zero energy and denoted by the dashed line.

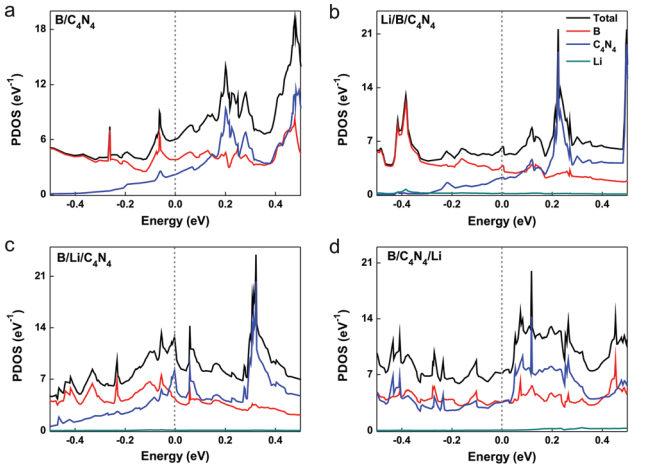

Fig. 5 Projected density of states (PDOS) of B/C_4N_4 vdW heterojunctions (a) before and (b–d) after Li-ion adsorption at the top, sandwiched, and bottom sites, respectively. The Fermi level is set at zero energy and denoted by the dashed line.

A large Schottky barrier height (SBH) impedes the interlayer electronic transport and degrades the performance of a photodiode based on the p–n junction. The homogeneous stacking of materials in the bottom and upper sublayers makes B/B and C_4N_4/C_4N_4 vdW homojunctions inappropriate to build p–n junctions, from the point of view of photodiode application. When using borophene and C_4N_4 monolayers as the left and right electrodes, it will be very important to explore the interfacial Schottky barrier height (Φ_S) in B/C_4N_4 vdW heterojunctions before and after Li-ions adsorption. Φ_S is defined by the difference between the CBM/VBM of the C_4N_4 sublayer and the Fermi level (E_F) of the borophene sublayer and can be attained from the band structures of B/C_4N_4 vdW heterojunctions.[45] The vertical electron SBH (Φ_S^e) in B/C_4N_4 vdW heterojunctions is 0.013 eV, whereas the vertical hole SBH (Φ_S^h) is 1.06 eV, forming an n-type Schottky contact. As shown in the enlarged band structure near E_F in Fig. 4d, the adsorption of Li-ions at the top site has decreased the vertical Φ_S^e to zero, since the CBM of C_4N_4 has shifted downward to lower than E_F, while keeping Φ_S^h unchanged. By changing the adsorption of Li-ions from the top to the sandwiched site, the vertical Φ_S^h has been dramatically reduced to 0.05 eV. Furthermore, in the $B/C_4N_4/Li$ vdW heterojunction, both the CBM and VBM projected on C_4N_4 are shifted across E_F, thus resulting in zero Schottky barrier. Therefore, the Schottky contact between C_4N_4 and borophene can be effectively tuned into Ohmic contact, *via* optimizing the adsorption site of Li-ions. By comparing the band structures of B/C_4N_4 vdW heterojunctions with Li-ions on different adsorption sites, it is observed that CBM across E_F in $B/C_4N_4/Li$ is mainly contributed by C_4N_4, whereas that in $Li/B/C_4N_4$ is dominated by borophene. This is largely due to the stronger charge transfer between Li-ions and the sublayer in direct contact. The projected density of states (PDOS) in Fig. 5 indicates that the bottom C_4N_4 sublayer becomes more metallized, by moving down the adsorption site of Li-ions in the B/C_4N_4 vdW heterojunctions. Accordingly, the Fermi level is dominated by C_4N_4, which further validates the leading role of C_4N_4 in the n-type Ohmic contact between borophene and C_4N_4 in $B/C_4N_4/Li$. Such n-type Ohmic contact is highly desirable to the application of vdW heterojunctions in high-performance electronic and optoelectronic devices, because it can promote the electronic transport efficiency.[56,57]

There also exists another type of vertical energy barrier in the above B/C_4N_4 vdW heterojunctions, namely, the tunneling barrier. Different from the Schottky barrier, electrons and holes can be effectively separated with less energy loss in the tunneling barrier, thus generating photoelectric conversion.[58–60] Generally, the tunneling barrier height is dependent on the asymmetry of the heterojunction and can be evaluated by the Hartree difference potential (δV_H).[61,62] Herein, δV_H is calculated from the electron difference density as:

$$\nabla^2 \delta V_H[\delta n](r) = -\frac{e^2}{4\pi\varepsilon_0}\delta n(r), \quad (6)$$

with the electron difference density $\delta n(r)$ being defined through the relation:

$$n(r) = \delta n(r) + \sum_I^{N_{atoms}} n_I(r), \quad (7)$$

where $n_I(r)$ is the compensation charge of atom I and N_{atoms} is the number of atoms in the system. Fig. 6a demonstrates the change of δV_H in bilayer systems, by changing the type of material in the

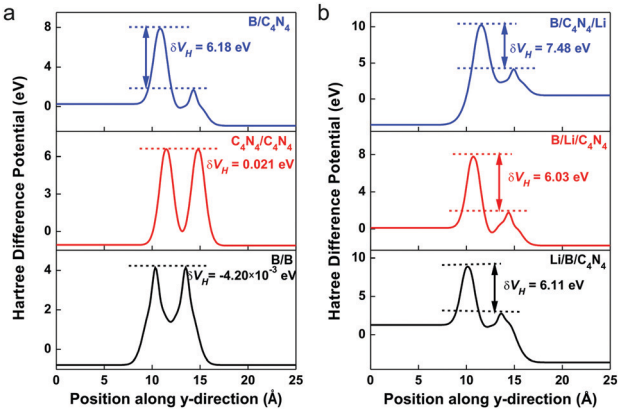

Fig. 6 The interlayer Hartree difference potentials for (a) bilayer systems consisting of borophene and C_4N_4 monolayers, and (b) B/C_4N_4 vdW heterojunctions with Li-ions at the top, sandwiched, and bottom adsorption sites, respectively.

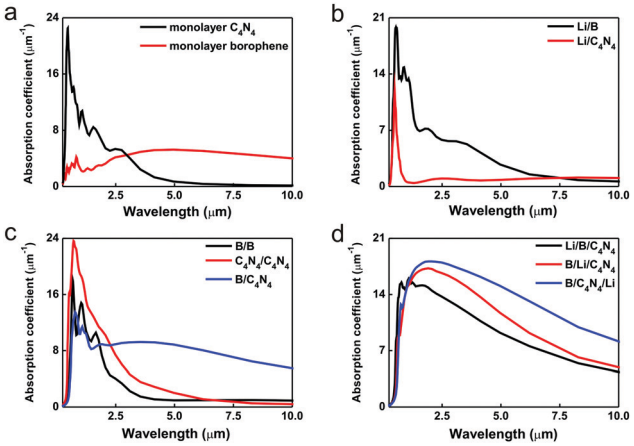

Fig. 7 Optical absorption spectra for borophene and C_4N_4 monolayers (a) before and (b) after Li-ion adsorption, (c) bilayer systems consisting of borophene and C_4N_4, and (d) B/C_4N_4 vdW heterojunctions with Li-ions on various adsorption sites, respectively.

sublayer. δV_H in B/B and C_4N_4/C_4N_4 vdW homojunctions is nearly zero, revealing that the structure with high symmetry is not applicable in optoelectronic nanodevices. In contrast, δV_H in the B/C_4N_4 vdW heterojunction has reached 6.18 eV, owing to the strong interlayer separation of hole–electron pairs. Furthermore, its δV_H value can be modulated from 6.11 eV in Li/B/C_4N_4 to 7.48 eV in B/C_4N_4/Li, showing that the adsorption of Li-ions on the bottom site can improve the asymmetry of B/C_4N_4 vdW heterojunctions most significantly. In contrast, the adsorption of Li-ions on the sandwiched site decreases the δV_H value to 6.03 eV, which weakens the structure asymmetry. Thereupon, B/C_4N_4/Li possesses the highest tunneling barrier, making it the optimal unit for photodiode applications.

We further calculated the optical absorption coefficients in various bilayer systems in comparison with isolated borophene and C_4N_4 monolayers. Normally, a wide direct bandgap can induce larger probabilities of electron migration under illumination. As shown in Fig. 7a and b, the adsorption of Li-ions on monolayer C_4N_4 severely suppresses its high absorption peak (>23.55 μm^{-1}) in a wide solar spectrum from the ultraviolet region (0.29 μm) to the mid-infrared (2.76 μm), due to the disappearance of the bandgap in Li/C_4N_4. In contrast, the optical absorption peak of pristine borophene in the range from 0.25 to 0.83 μm has been remarkably intensified nearly 5 times by the adsorption of Li-ions and extended from the near-infrared to mid-infrared region as far as >7.48 μm, since the adsorbed Li-ions on the borophene substrate provide states shallower than that in the Li/C_4N_4 system. As for the formation of a bilayer structure, the wide bandgap in C_4N_4/C_4N_4 vdW homojunctions results in its sharp optical absorption peak in the visual region, whereas the higher tunneling barrier in B/C_4N_4 vdW heterojunctions leads to its wider optical absorption peak in the entire infrared region (>1.46 μm). The integral area ratio of infrared light reaches nearly 50% in the solar radiation spectrum, much larger than those of ultraviolet and visual lights. The strong optical response under infrared illumination allows the B/C_4N_4 vdW heterojunctions to make the best use of sunlight. In view of the poor infrared-light capturing capabilities, B/B and C_4N_4/C_4N_4 vdW homojunctions will not be considered in the following electronic transport behavior study for photodiode applications. In B/C_4N_4 vdW heterojunctions with Li-ion adsorption, the optical absorption peak has been enhanced by approximately 14% without a remarkable shift, by changing the adsorption site from the top to the bottom, since the tunneling barrier becomes higher. Therefore, the adsorption of Li-ions on the bottom site provides a feasible method to enhance its optical absorption, which would be conducive to improving the performance of optoelectronic nanodevices based on B/C_4N_4 vdW heterojunctions.

The effect of tunneling barrier on the device performance of a photodiode based on B/C_4N_4 vdW heterojunctions can also be reflected by the change of its quantum transport behavior *via* Li-ion adsorption. Fig. 8a displays the schematic diagram of a two-probe B/C_4N_4 vdW heterojunction system with Li-ion adsorption, in which the Li-ion adsorption can be manipulated between the top, sandwiched, and bottom sites. In the central region, the supercell of B/C_4N_4 vdW heterojunctions repeats twice along the *z*-direction, *i.e.* the direction of the electric field.

We plot the current–bias (I–V_b) dependence curves of B/C_4N_4 vdW heterojunctions with different Li-ions adsorption sites in Fig. 8b. In B/C_4N_4 vdW heterojunction without the adsorption of Li-ions, the reverse current (-1.0 to 0 V) decreases rapidly, which is much more remarkable than the forward one (1.0 to 0 V), by descending $|V_b|$. As a result, B/C_4N_4 shows an obvious negative rectification behavior. To quantitatively illustrate the rectifying behavior, we define the rectifying ratio (R) as $R = |I(-V_b)/I(+V_b)|$. $R = 1$ indicates no rectification effect, and $R > 1$ denotes a higher reverse current, *i.e.* a negative rectification, whereas $R < 1$ represents a higher forward current, known as a positive rectification.[63,64] The V_b–R curves in B/C_4N_4 vdW heterojunctions with various Li-ion adsorption sites are shown in Fig. 8c. The R value of B/C_4N_4 vdW heterojunctions reaches the maximum of 3.68 at $|V_b| = 0.2$ V and the minimum of 0.60 at $|V_b| = 0.6$ V. The

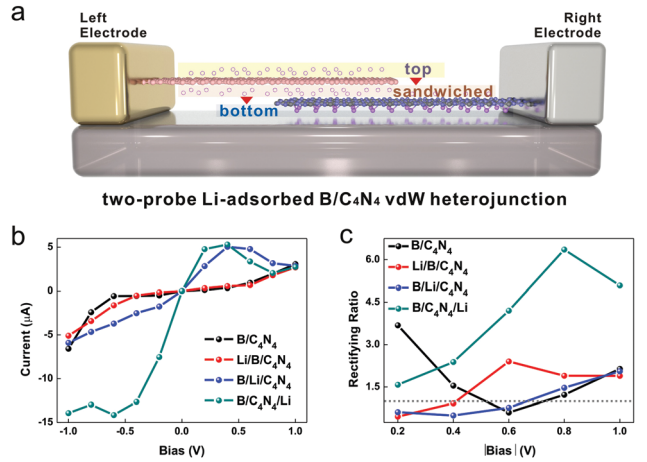

Fig. 8 (a) Schematic diagram of two-probe B/C_4N_4 vdW heterojunction with Li-ion adsorption, in which the adsorption varies between the top and bottom sites. (b) The dependence of current and (c) the rectifying ratio on bias voltage in B/C_4N_4 vdW heterojunctions before and after Li-ion adsorption, respectively.

reversed rectifying status in B/C_4N_4 reveals that the metallic-semiconductive asymmetry is tunable by changing the direction of the electric field. The R value in $Li/B/C_4N_4$ vdW heterojunctions shows the opposite tendency with rising $|V_b|$, in which the minimum is 0.46 at $|V_b| = 0.2$ V and the maximum is 2.40 at $|V_b| = 0.6$ V. It is indicated that the sandwiched-adsorption of Li-ions can reverse the metallic-semiconductive asymmetry.

An obvious negative differential resistance (NDR) effect under forward bias arises in $B/Li/C_4N_4$ and $B/C_4N_4/Li$ vdW heterojunctions, making them competitive candidate structures for Esaki diodes, which are used as static random access memories, multivalued logic circuits, and so on.[65–68] Their peak and valley of the current are located at $V_b = 0.4$ V and 0.8–1.0 V, respectively, resulting in an increase of peak-to-valley ratio (PVR) from 1.76 to 2.60. In the meantime, the reverse current is apparently enhanced and also shows an NDR effect in $B/C_4N_4/Li$, when the reverse V_b rises to higher than −0.6 V. Its R value increases from 1.58 to 6.38 when $|V_b|$ rises from 0.2 to 0.8 V and then decreases to 5.09 at $|V_b| = 1.0$ V, due to the emergence of NDR effect under reverse bias. The maximum R value in $B/C_4N_4/Li$ is almost 2 times higher than those in B/C_4N_4 vdW heterojunctions with Li-ion adsorption on the other adsorption sites. The reason for this phenomenon might be that the injection of electrons from the adsorbed Li-ions to bottom C_4N_4 is so remarkable that the vdW heterojunction is transformed from metallic-semiconductor to metallic donor–acceptor. The separation of hole–electron pairs is much stronger than the former, consistent with the raised tunneling barrier as mentioned above. Such strong negative rectification in $B/C_4N_4/Li$ vdW heterojunctions can be applied to improve the photosensitivity in the dark and under infrared illumination conditions in tunneling photodiodes.[69–71]

In order to understand the tunable asymmetric transport behavior in B/C_4N_4 vdW heterojunctions *via* Li-ion adsorption, we explore the transport mechanism in two-probe Li-ion-adsorbed B/C_4N_4 systems. The transmission function $T(E,V_b)$ is the sum of transmission probabilities of all channels available at energy E under external bias voltage V_b:

$$T(E,V_b) = \mathrm{Tr}[\Gamma_L(V_b)G^R(E,V_b)\Gamma_R(V_b)G^A(E,V_b)], \quad (8)$$

where G^R and G^A are the retarded and advanced Green's functions, respectively, and the coupling functions Γ_L and Γ_R are the imaginary parts of the left and right self-energies, which depend on the surface Green's functions of the electrode regions and come from the nearest-neighbor interaction between the extended central region and the electrodes.

Fig. 9 gives the contour maps of transmission spectra for all B/C_4N_4 vdW heterojunctions before and after Li-ion adsorption from −1.0 to 1.0 eV at V_b from −1.0 to 1.0 V. The region within the yellow dashed lines is the bias window, where the current depends on the integral of $T(E,V_b)$. The blue color denotes a low transmission coefficient, whereas the red one represents a high transmission coefficient. Apparently, in B/C_4N_4 vdW heterojunctions, the transmission peak begins to appear in the bias window when $|V_b|$ increases to higher than 0.5 V, revealing that the observable current starts to flow through the heterojunction only after $|V_b| > 0.5$ V. In addition, the integral area of $T(E,V_b)$ in the reverse V_b region is much larger than that in the forward V_b region, thus leading to a negative rectification. It is most notable in $B/C_4N_4/Li$ vdW heterojunctions that the peaks in the reverse V_b region move positively to higher energy levels and the corresponding integral of $T(E,V_b)$ shows an increasing trend, by increasing $|V_b|$. Meanwhile, some peaks begin to emerge under a lower $|V_b|$. It is indicated that the increase of V_b can further strengthen the n-type doping effect of the adsorbed Li-ions on the C_4N_4 sublayer, which has modulated the C_4N_4 sublayer from hole-dominated semiconductive into electron-dominated metallic. A vast number of electrons are also withdrawn from the upper borophene to bottom C_4N_4. Eventually, the metallic donor–acceptor asymmetry in $B/C_4N_4/Li$ shows improved negative rectification

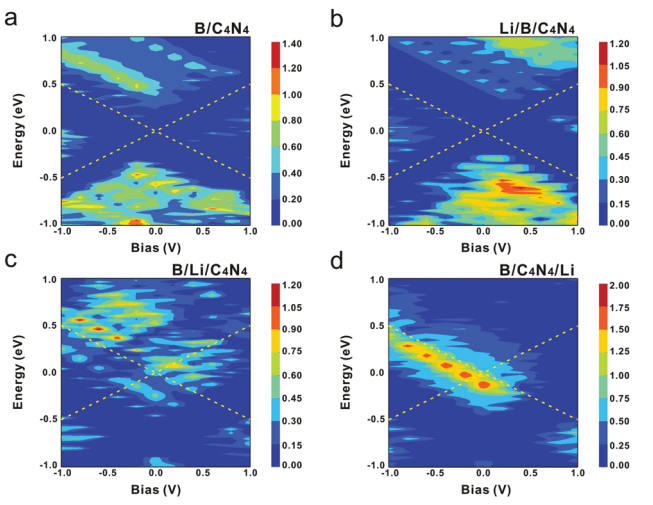

Fig. 9 The transmission coefficient contours as a function of energy and bias voltage in (a) B/C_4N_4, (b) $Li/B/C_4N_4$, (c) $B/Li/C_4N_4$, and (d) $B/C_4N_4/Li$ vdW heterojunctions, respectively. The region within the yellow dashed lines is the bias window.

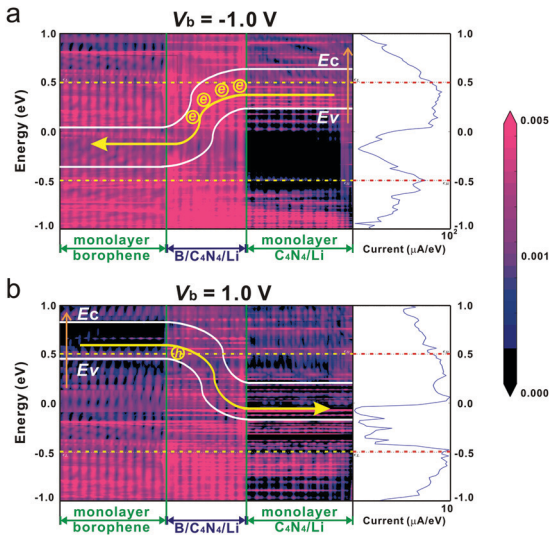

Fig. 10 Spatially resolved local density of states (LDOS) (left side) and the corresponding spectral current (right side) in B/C_4N_4/Li vdW heterojunctions at (a) V_b = −1.0 V and (b) V_b = 1.0 V, respectively.

behavior, enabling its promising applications in high-performance photodiodes.

To further analyze why B/C_4N_4/Li vdW heterojunctions have superior negative rectification behavior, its transport probability at V_b = −1.0 V is compared with that at V_b = 1.0 V. The projected local density of states (PLDOS) and spectral current of B/C_4N_4/Li vdW heterojunctions at V_b = −1.0 and 1.0 V are displayed in Fig. 10. In PLDOS, the bright block stands for the existence of DOS, whereas the dark one indicates the energy gap without DOS distribution. Borophene and C_4N_4/Li monolayers are separated by B/C_4N_4/Li vdW heterojunctions, as indicated by the green vertical line. It is worth noting that the current in B/C_4N_4/Li is mainly attributed to the transport behavior in the energy region higher than 0 eV, whether at −1.0 V or at 1.0 V. Nevertheless, the transport processes at V_b = −1.0 V and V_b = 1.0 V are quite different. V_b = −1.0 V implies a higher potential of the right C_4N_4/Li electrode, whereas V_b = 1.0 V means a higher potential of the left borophene electrode. At V_b = −1.0 V, CBM and VBM of the right C_4N_4/Li electrode are shifted upward relative to E_F and CBM of the left borophene electrode. The higher energy levels on the right C_4N_4/Li with respect to the left borophene provide enough channels for electrons to transport through B/C_4N_4/Li, as the current under negative bias starts to flow only after VBM of the right electrode reaches CBM of the left one.[72] The n-type Ohmic contact in the central B/C_4N_4/Li vdW heterojunction has no blocking effect on the transport efficiency. Numerous electrons are injected from the adsorbed Li-ions to the C_4N_4 monolayer, which plays the role of the majority carriers and promotes the interband tunneling from VBM of C_4N_4/Li to CBM of borophene, thereby resulting in a large reverse current at V_b = −1.0 V. The electron-withdrawing capability of bottom C_4N_4 in B/C_4N_4/Li is so strong that it can not only accept electrons from Li-ions but also from upper borophene. As a result, VBM of borophene is occupied by holes, which play as the majority carriers under the forward bias. At V_b = 1.0 V, the higher potential of the left borophene electrode has significantly shifted the CBM and VBM of borophene upward to higher than the E_F and CBM of the right C_4N_4/Li. Consequently, the holes on VBM of the left borophene move to CBM of the right C_4N_4/Li with relatively low energy, bringing about the forward current. In comparison with the high electron concentration in C_4N_4/Li, the lower hole concentration in borophene has suppressed the forward current. Therefore, the large difference in carrier concentrations on the upper borophene and bottom C_4N_4/Li layers of B/C_4N_4/Li vdW heterojunctions is the origin of its high interlayer tunneling barrier, on which superior negative rectification behavior is generated. This will be of great importance to the application of B/C_4N_4/Li vdW heterojunctions in high-performance optoelectronic devices, such as photodetectors and photodiodes.

4. Conclusions

In conclusion, we have developed a new strategy to eliminate the interlayer Schottky barrier in B/C_4N_4 vdW heterojunctions and finally realized the Ohmic contact between borophene and C_4N_4, through the combination of vertical stacking and Li-ion adsorption. The remarkable separation of hole–electron pairs in B/C_4N_4 vdW heterojunctions makes it superior to B/B and C_4N_4/C_4N_4 vdW heterojunctions as the candidate structure for photodiode application. The adsorption of Li-ions on B/C_4N_4 vdW heterojunctions can not only eliminate the Schottky barrier but also increase the tunneling barrier by modulating the adsorption site from top to bottom, achieving an n-type Ohmic contact, which is largely attributed to the enhanced electron injection into the C_4N_4 sublayer. B/C_4N_4/Li exhibits the most excellent absorbing capability of the infrared illumination and the strongest negative rectification, among a series of Li-adsorbed B/C_4N_4 vdW heterojunctions, showing great potential in tunneling photodiode applications. Both the transmission spectra and PLDOS demonstrate that the largest difference in carrier concentrations on the left and right electrodes is the origin of the highest tunneling barrier in the two-probe B/C_4N_4/Li system at reverse and forward bias, thus resulting in the largest rectifying ratio. Our study is expected to encourage experimental realization of the tunneling photodiode based on vdW heterojunction with Ohmic contact.

Author contributions

Cancan Zheng, Man Shi, Haiyan Li, Nianxi Dou, and Zhihao Ma: Data curation; Cong Zhou: Validation; FeiFei Xia: Visualization; Yuanyuan He: Conceptualization, investigation, and writing original draft; Jianwei Zhao: Methodology, software, and supervision.

Conflicts of interest

There are no conflicts to declare.

Acknowledgements

This work was supported by the National Natural Science Foundation of China (Grant No. 51802121, and 51861145202), Jiaxing Science and Technology Project (Grant No. 2020AY10008, and 2020AD10017), the Student Research Training Program of Jiaxing University (CD8517203297), and the Open Project Program of Key Laboratory of Yarn Materials Forming and Composite Processing Technology, Zhejiang Province, Jiaxing University (MTC2020-17).

References

1 C. Y.-P. Chao, S.-F. Yeh, M.-H. Wu, K.-Y. Chou, T. Honyih, C.-L. Lee, C. Yin, P. Paillet and V. Goiffon, *Sensors*, 2019, **19**, 5447.
2 Z. Liu, S. Li, Z. Y. Yan, Y. Y. Liu, Y. S. Zhi, X. Wang, Z. P. Wu, P. G. Li and W. H. Tang, *J. Mater. Chem. C*, 2020, **8**, 5071–5081.
3 P. E. Malinowski, E. Georgitzikis, J. Maes, I. Vamvaka, F. Frazzica, J. Van Olmen, P. De Moor, P. Heremans, Z. Hens and D. Cheyns, *Sensors*, 2017, **17**, 2867.
4 W. Chen, B. Chen, A. Holmes and P. Fay, *Electron. Lett.*, 2015, **51**, 1439–1440.
5 M. Mazzillo, G. Condorelli, M. E. Castagna, G. Catania, A. Sciuto, F. Roccaforte and V. Raineri, *IEEE Photonics Technol. Lett.*, 2009, **21**, 1782–1784.
6 B. Jeon, H. Lee, K. C. Goddeti and J. Y. Park, *ACS Appl. Mater. Interfaces*, 2019, **11**, 15152–15159.
7 J. Y. Xu, J. S. Yu, J. H. Liao, X. B. Yang, C. Y. Wu, Y. Wang, L. Wang, C. Xie and L. B. Luo, *ACS Appl. Mater. Interfaces*, 2019, **11**, 21702–21710.
8 L. H. Zeng, M. Z. Wang, H. Hu, B. Nie, Y. Q. Yu, C. Y. Wu, L. Wang, J. G. Hu, C. Xie, F. X. Liang and L. B. Luo, *ACS Appl. Mater. Interfaces*, 2013, **5**, 9362–9366.
9 B. Mukherjee, A. Zulkefli, R. Hayakawa, Y. Wakayama and S. Nakaharai, *ACS Photonics*, 2019, **6**, 2277–2286.
10 A. Allain, J. H. Kang, K. Banerjee and A. Kis, *Nat. Mater.*, 2015, **14**, 1195–1205.
11 M. Buscema, J. O. Island, D. J. Groenendijk, S. I. Blanter, G. A. Steele, H. S. J. van der Zant and A. Castellanos-Gomez, *Chem. Soc. Rev.*, 2015, **44**, 3691–3718.
12 X. Zhou, X. Z. Hu, S. S. Zhou, H. Y. Song, Q. Zhang, L. J. Pi, L. Li, H. Q. Li, J. T. Lu and T. Y. Zhai, *Adv. Mater.*, 2018, **30**, 1703286.
13 T. T. Li, C. He and W. X. Zhang, *J. Mater. Chem. A*, 2019, **7**, 4134–4144.
14 R. Longuinhos and J. Ribeiro-Soares, *Physica E*, 2020, **119**, 114007.
15 S. W. Yang, W. Li, C. C. Ye, G. Wang, H. Tian, C. Zhu, P. He, G. Q. Ding, X. M. Xie, Y. Liu, Y. Lifshitz, S. T. Lee, Z. H. Kang and M. H. Jiang, *Adv. Mater.*, 2017, **29**, 1605625.
16 Y. W. Li, S. H. Zhang, J. B. Yu, Q. Wang, Q. Sun and P. R. Jena, *Nano Res.*, 2015, **8**, 2901–2912.
17 J. Mahmood, E. K. Lee, M. Jung, D. Shin, I. Y. Jeon, S. M. Jung, H. J. Choi, J. M. Seo, S. Y. Bae, S. D. Sohn, N. Park, J. H. Oh, H. J. Shin and J. B. Baek, *Nat. Commun.*, 2015, **6**, 6486.
18 J. Li, C. Cao, J. Hao, H. Qiu, Y. Xu and H. Zhu, *Diamond Relat. Mater.*, 2006, **15**, 1593–1600.
19 L. Z. Liu, S. J. Xiong and X. L. Wu, *Appl. Phys. Lett.*, 2016, **109**, 061601.
20 D. Yin and Y. Yoon, *J. Appl. Phys.*, 2016, **119**, 214312.
21 M. L. Geier, K. Moudgil, S. Barlow, S. R. Marder and M. C. Hersam, *Nano Lett.*, 2016, **16**, 4329–4334.
22 S. D. Lei, X. F. Wang, B. Li, J. H. Kang, Y. M. He, A. George, L. H. Ge, Y. J. Gong, P. Dong, Z. H. Jin, G. Brunetto, W. B. Chen, Z. T. Lin, R. Baines, D. S. Galvao, J. Lou, E. Barrera, K. Banerjee, R. Vajtai and P. Ajayan, *Nat. Nanotechnol.*, 2016, **11**, 465–471.
23 Y. Y. He, F. F. Xia, Z. B. Shao, J. W. Zhao and J. S. Jie, *J. Phys. Chem. Lett.*, 2015, **6**, 4701–4710.
24 Y. H. Li, Y. A. Deng, J. F. Zhang, Y. Y. Shen, X. Y. Yang and W. W. Zhang, *J. Alloys Compd.*, 2020, **842**, 155985.
25 Y. C. Huang, D. M. Zhou, X. Chen, H. Liu, C. Wang and S. F. Wang, *ChemPhysChem*, 2016, **17**, 375–379.
26 S. Susarla, V. Kochat, A. Kutana, J. A. Hachtel, J. C. Idrobo, R. Vajtai, B. I. Yakobson, C. S. Tiwary and P. M. Ajayan, *Chem. Mater*, 2017, **29**, 7431–7439.
27 L. Nguyen, H. P. Komsa, E. Khestanova, R. J. Kashtiban, J. J. P. Peters, S. Lawlor, A. M. Sanchez, J. Sloan, R. V. Gorbachev, I. V. Grigorieva, A. V. Krasheninnikov and S. J. Haigh, *ACS Nano*, 2017, **11**, 2894–2904.
28 T. Liu, S. Liu, K. H. Tu, H. Schmidt, L. Q. Chu, D. Xiang, J. Martin, G. Eda, C. A. Ross and S. Garaj, *Nat. Nanotechnol.*, 2019, **14**, 223–226.
29 Y. Zhang, C. H. Liu, J. B. Liu, J. Xiong, J. Y. Liu, K. Zhang, Y. D. Liu, M. Z. Peng, A. F. Yu, A. H. Zhang, Y. Zhang, Z. W. Wang, J. Y. Zhai and Z. L. Wang, *ACS Appl. Mater. Interfaces*, 2016, **8**, 1381–1387.
30 M. Ke, N. Huu Duy, H. Fan, M. Li, H. Wu and Y. Hu, *Nano Res.*, 2020, **13**, 1369–1375.
31 Z. Jia, J. Shi, Q. Shang, W. Du, X. Shan, B. Ge, J. Li, X. Sui, Y. Zhong, Q. Wang, L. Bao, Q. Zhang and X. Liu, *ACS Appl. Mater. Interfaces*, 2019, **11**, 20566–20573.
32 Y. Ou, Z. Kang, Q. L. Liao, S. H. Gao, Z. Zhang and Y. Zhang, *Nanoscale*, 2020, **12**, 9859–9865.
33 X. K. Zhang, Q. L. Liao, Z. Kang, B. S. Liu, Y. Ou, J. L. Du, J. K. Xiao, L. Gao, H. Y. Shan, Y. Luo, Z. Y. Fang, P. D. Wang, Z. Sun, Z. Zhang and Y. Zhang, *ACS Nano*, 2019, **13**, 3280–3291.
34 M. Brandbyge, J. L. Mozos, P. Ordejon, J. Taylor and K. Stokbro, *Phys. Rev. B: Condens. Matter Mater. Phys.*, 2002, **65**, 165401.
35 C. Riplinger and F. Neese, *J. Chem. Phys.*, 2013, **138**, 034106.
36 S. Grimme, J. Antony, S. Ehrlich and H. Krieg, *J. Chem. Phys.*, 2010, **132**, 154104.
37 M. Schlipf and F. Gygi, *Comput. Phys. Commun.*, 2015, **196**, 36–44.
38 L. G. Ferreira, M. Marques and L. K. Teles, *Phys. Rev. B*, 2008, **78**, 125116.
39 L. G. Ferreira, M. Marques and L. K. Teles, *AIP Adv.*, 2011, **1**, 032119.
40 R. Landauer, *IBM J. Res. Dev.*, 1988, **32**, 306–316.

41 M. Büttiker, *Phys. Rev. Lett.*, 1986, **57**, 1761–1764.
42 N. A. Vinogradov, A. Lyalin, T. Taketsugu, A. S. Vinogradov and A. Preobrajenski, *ACS Nano*, 2019, **13**, 14511–14518.
43 V. Bezugly, J. Kunstmann, B. Grundkotter-Stock, T. Frauenheim, T. Niehaus and G. Cuniberti, *ACS Nano*, 2011, **5**, 4997–5005.
44 D. Liu and D. Tomanek, *Nano Lett.*, 2019, **19**, 1359–1365.
45 J. H. Yan, X. Y. Zhang, Y. Y. Pan, J. Z. Li, B. W. Shi, S. Q. Liu, J. Yang, Z. G. Song, H. Zhang, M. Ye, R. G. Quhe, Y. Y. Wang, J. B. Yang, F. Pan and J. Lu, *J. Mater. Chem. C*, 2018, **6**, 6153–6163.
46 M. Yousaf, Y. S. Wang, Y. J. Chen, Z. P. Wang, A. Firdous, Z. Ali, N. Mahmood, R. Q. Zou, S. J. Guo and R. P. S. Han, *Adv. Energy Mater.*, 2019, **9**, 1900567.
47 Y. F. Li, Y. L. Liang, F. C. R. Hernandez, H. D. Yoo, Q. Y. An and Y. Yao, *Nano Energy*, 2015, **15**, 453–461.
48 J. M. Liao, B. S. Sa, J. Zhou, R. Ahuja and Z. M. Sun, *J. Phys. Chem. C*, 2014, **118**, 17594–17599.
49 X. Li, W. Liu, B. Huang, H. Liu and X. Li, *J. Mater. Chem. C*, 2020, **8**, 15804–15815.
50 R. Moradian, M. Shahrokhi, S. S. Charganeh and S. Moradian, *Physica E*, 2012, **46**, 182–188.
51 H. Guo, Z. Zhang, B. Huang, X. Wang, H. Niu, Y. Guo, B. Li, R. Zheng and H. Wu, *Nanoscale*, 2020, **12**, 20025–20032.
52 X. G. Ma, J. S. Hu, H. He, S. J. Dong, C. Y. Huang and X. B. Chen, *ACS Appl. Nano Mater.*, 2018, **1**, 5507–5515.
53 V. Shukla, J. Wärnå, N. K. Jena, A. Grigoriev and R. Ahuja, *J. Phys. Chem. C*, 2017, **121**, 26869–26876.
54 F. F. Xia, S. Y. Xiong, Y. Y. He, Z. B. Shao, X. J. Zhang and J. S. Jie, *J. Phys. Chem. C*, 2017, **121**, 19530–19537.
55 Z. Wang, Y. Zhang, X. Wei, T. T. Guo, J. B. Fan, L. Ni, Y. J. Weng, Z. D. Zha, J. Liu, Y. Tian, T. Li and D. Li, *Phys. Chem. Chem. Phys.*, 2020, **22**, 9647–9655.
56 H. M. Hu, Z. Zhang and G. Ouyang, *Appl. Surf. Sci.*, 2020, **517**, 146168.
57 Y. G. Guo, W. A. Saidi and Q. Wang, *2D Mater.*, 2017, **4**, 035009.
58 C. C. Jia, W. Ma, C. H. Gu, H. L. Chen, H. M. Yu, X. X. Li, F. Zhang, L. Gu, A. D. Xia, X. Y. Hou, S. Meng and X. F. Guo, *Nano Lett.*, 2016, **16**, 3600–3606.
59 R. Oshima, Y. Shoji, K. Makita, A. Ubukata and T. Sugaya, *IEEE J. Photovoltaics*, 2020, **10**, 749–753.
60 S. M. Lu, X. Guan, X. C. Li, J. Liu, F. Huang and W. C. H. Choy, *Nano Energy*, 2016, **21**, 123–132.
61 J. B. Wu, H. Y. Chen, N. Yang, J. Cao, X. D. Yan, F. X. Liu, Q. B. Sun, X. Ling, J. Guo and H. Wang, *Nat. Electron.*, 2020, **3**, 466–472.
62 T. M. Abdolkader, A. Shaker and A. N. M. Alahmadi, *Eur. J. Phys.*, 2018, **39**, 045402.
63 Y. Y. He, C. Chen, N. Cheng, S. Y. Xiong and J. W. Zhao, *Sci. China: Technol. Sci.*, 2019, **62**, 478–489.
64 J. W. Zhao, N. Cheng and Y. Y. He, *Phys. Chem. Chem. Phys.*, 2019, **21**, 19567–19574.
65 L. Esaki, *IEEE Trans. Electron Devices*, 1976, **23**, 644–647.
66 K. Kobashi, R. Hayakawa, T. Chikyow and Y. Wakayama, *Adv. Electron. Mater.*, 2017, **3**, 1700106.
67 L. Wang, J. M. L. Figueiredo, C. N. Ironside and E. Wasige, *IEEE T. Electron. Dev*, 2011, **58**, 343–347.
68 Y. Wakayama and R. Hayakawa, *Adv. Funct. Mater.*, 2020, **30**, 1903724.
69 F. Wu, H. Xia, H. D. Sun, J. W. Zhang, F. Gong, Z. Wang, L. Chen, P. Wang, M. S. Long, X. Wu, J. L. Wang, W. C. Ren, X. S. Chen, W. Lu and W. D. Hu, *Adv. Funct. Mater.*, 2019, **29**, 1900314.
70 J. Singh, R. G. Singh, S. K. Gautam and F. Singh, *J. Appl. Phys.*, 2018, **123**, 174503.
71 A. Echresh, M. Echresh, V. Khranoyskyy, O. Nur and M. Willander, *J. Lumin.*, 2016, **178**, 324–330.
72 Y. Y. He, N. Cheng, C. Chen, S. Y. Xiong and J. W. Zhao, *Sci. China-Technol. Sci*, 2019, **62**, 799–810.